

# Unifying domain adaptation and self-supervised learning for CXR segmentation via AdaIN-based knowledge distillation

Yujin Oh<sup>a,1</sup>, Jong Chul Ye<sup>a,\*</sup>

<sup>a</sup>Korea Advanced Institute of Science and Technology (KAIST), Daejeon, South Korea

## ARTICLE INFO

2000 MSC: 41A05, 41A10, 65D05, 65D17

**Keywords:** Segmentation, Self-supervised learning, Domain adaptation, Knowledge distillation, Chest X-ray.

## ABSTRACT

As the segmentation labels are scarce, extensive researches have been conducted to train segmentation networks without labels or with only limited labels. In particular, semi-supervised domain adaptation and self-supervised learning have been introduced to distill knowledge from various tasks to improve the segmentation performance. However, these approaches appear different from each other, so it is not clear how these seemingly different approaches can be combined for better performance. Inspired by the recent StarGANv2 for multi-domain image translation, here we propose a novel segmentation framework via AdaIN-based knowledge distillation, where a single generator with AdaIN layers is trained along with the AdaIN code generator and style encoder so that the generator can perform both domain adaptation and segmentation. Specifically, our framework is designed to deal with difficult situations in chest X-ray (CXR) segmentation tasks where segmentation masks are only available for normal CXR data, but the trained model should be applied for both normal and abnormal CXR images. Since a single generator is used for abnormal to normal domain conversion and segmentation by simply changing AdaIN codes, the generator can synergistically learn the common features to improve segmentation performance. Experimental results using CXR data confirm that the trained network can achieve the state-of-the-art segmentation performance for both normal and abnormal CXR images.

© 2021

## 1. Introduction

High-accuracy image segmentation often serve as the first step in various medical imaging tasks (De Fauw et al., 2018; Ouyang et al., 2020). Recently, deep learning (DL) approaches have become the state-of-the-art (SOTA) techniques for medical image segmentation tasks thanks to their superior performance compared to the classical methods (De Fauw et al., 2018).

The performance of DL-based segmentation algorithms usually depends on large amount of labels, but segmentation masks are scarce due to the expensive and time-consuming annotation procedure. Another difficulty in DL-based medical image segmentation is the so-called domain shift, i.e., a segmentation network trained with data in a specific domain often undergoes drastic performance degradation when applied to unseen test domains.

For example, in chest X-ray (CXR) lung segmentation for infectious disease diagnosis, segmentation network trained with

normal CXR data often produce under-segmentation when applied to abnormal CXR images from severe infectious diseases such as bacterial pneumonia (Oh et al., 2020). The missed regions from under-segmentation mostly contain crucial features, such as pulmonary consolidations, for diagnosing infectious disease. Thus, highly-accurate segmentation without under-segmentation for both normal and abnormal lung CXR is required to guarantee that DL-based classification algorithms fully learn entire lung features while alleviating irrelevant factors outside the lung.

To solve the label scarcity and domain shift problems, there have been extensive researches to train segmentation networks in a semi-supervised manner using limited training labels, or even without labeled dataset in a self-supervised or unsupervised manner (Bai et al., 2017; Tang et al., 2019; Chen et al., 2020; Perone et al., 2019). For example, teacher-student architecture and domain adaptation have been introduced to take advantages of learned features from the supervised learning tasks, and distillate the knowledge to unsupervised learning tasks (Li et al., 2020a). However, these approaches appear different from each other, and there exist no consensus in regard to how these different approaches can be synergistically combined.

\*Corresponding author: Tel.: +82-042-350-4320; fax: +82-42-350-4310; e-mail: jong.ye@kaist.ac.kr (Jong Chul Ye)

Inspired by the success of StarGANv2 for image style transfer between various domains (Choi et al., 2020), here we propose a unified knowledge distillation framework that can synergistically combine domain adaptation, self-supervised and supervised training to provide improved segmentation. Specifically, our framework is designed to deal with difficult but often encountered situations where segmentation masks are only available for normal data, but the trained method should be applied for both normal and abnormal images.

The key idea of the proposed method is that a single generator trained along with the adaptive instance normalization (AdaIN) (Huang and Belongie, 2017) can perform segmentation for normal data as well as domain adaptation between normal and abnormal domains, by simply changing the AdaIN codes. The network is also trained in a self-supervised manner in order to force the direct segmentation results to match the other segmentation results through domain adaptation and subsequent segmentation. Then, direct segmentation of abnormal images can be performed accurately using another AdaIN code. Since a single generator is used for all these tasks by simply changing the AdaIN codes, the network can synergistically learn the common features from all tasks through knowledge distillation.

To validate the concept of the proposed framework, we train our network using labeled normal chest X-ray (CXR) data with unlabeled pneumonia CXR dataset, and test the model performance on unseen dataset composed of COVID-19 pneumonia CXR images (Borghesi and Maroldi, 2020; de la Iglesia Vayá et al., 2020). Experimental results confirmed that our method can achieve SOTA performance for abnormal CXR segmentation.

The remainder of this paper is organized as follow. Section 2 summarizes the related works. Section 3 and Section 4 describes the proposed framework and methods, respectively. Experimental results are presented in Section 5. Finally, we discuss and conclude this work in Section 6 and Section 7, respectively.

## 2. Related Works

To make this paper self-contained, here we review several existing works that are necessary to understand our method.

### 2.1. Image style transfer

The aim of the image style transfer is to convert the content images into certain stylized images. Currently, two types of approaches are most often used for image style transfer.

First, a content image and a style reference image are passed to a neural network, and the goal is to convert the content image to imitate styles from the style reference. For example, the adaptive instance normalization (AdaIN) was proposed as a simple but powerful method (Huang and Belongie, 2017). Specifically, AdaIN layer estimates the means and standard deviation (std) of referenced style features and uses them to correct those of the content features. For example, (Huang et al., 2018) introduced a multimodal unsupervised image-to-image translation (MUNIT), which decompose an image into content

and style codes, and the encoded style codes for the desired domain replace affine parameters of the AdaIN layers in the decoder.

On the other hand, unsupervised style transfer approaches such as cycleGAN (Zhu et al., 2017) learn the target data distribution rather than a single style image. Unfortunately, the cycleGAN approach requires  $N(N - 1)$  generator to enable the translation between  $N$  domains. To deal with this, multi-domain image translation approaches have been proposed. In particular, StarGANv2 (Choi et al., 2020) introduced an advanced single generator-based framework, which transfers styles over multiple domains by changing domain-specific style codes of AdaIN layers.

### 2.2. Semi-supervised learning via domain adaptation

In domain adaptation approaches for medical image segmentation, a DL-based model trained with labeled dataset in a specific domain (e.g. normal CXR) is refined for different domain dataset in semi-supervised, self-supervised or unsupervised manners (Bai et al., 2017; Tang et al., 2019; Tarvainen and Valpola, 2017; Li et al., 2020a; Perone et al., 2019; Xue et al., 2020; Orbes-Arteaga et al., 2019; Li et al., 2020b; Chen et al., 2020). These approaches try to take advantages of learned features from the supervised learning in a specific domain, and distillate the knowledge to unsupervised learning tasks in unseen domains. Specifically, (Bai et al., 2017) applied a semi-supervised learning approach on cardiac MR image segmentation task and achieved higher performance compared to supervised baseline models, by alternatively generating pseudo-labels for unlabeled dataset with pre-trained model, and training the network on both labeled and pseudo-labeled dataset, continuously. (Tang et al., 2019) introduced a semi-supervised approach on pneumonia lung segmentation tasks, by generating pseudo-images via an image-to-image style transfer framework, followed by training another segmentation network with both labeled and pseudo-labeled dataset.

### 2.3. Teacher-Student approaches

Teacher-student framework consists of two individual networks, i.e., a student and a teacher model. The student model is trained in a supervised manner, as well as trained in a self-supervised manner which enforces the student model output to be consistent with outputs from the teacher model with unlabeled dataset (Tarvainen and Valpola, 2017; Li et al., 2020a; Perone et al., 2019).

Specifically, (Li et al., 2020a) introduced a dual-teacher framework on segmentation task, which consist of two teacher models: a traditional teacher model for intra-domain knowledge and an additional teacher model for inter-domain knowledge distillation. To leverage inter-domain dataset with segmentation label, images from domain-shifted dataset are style-transferred as pseudo-images. The additional inter-domain teacher, trained in a supervised manner with pseudo-labeled images, and the student are enforced to predict consistent output given the style-transferred images. Thus, the main goal is to make the student model fully leverage information from labeled, unlabeled and pseudo-labeled inter-domain dataset.

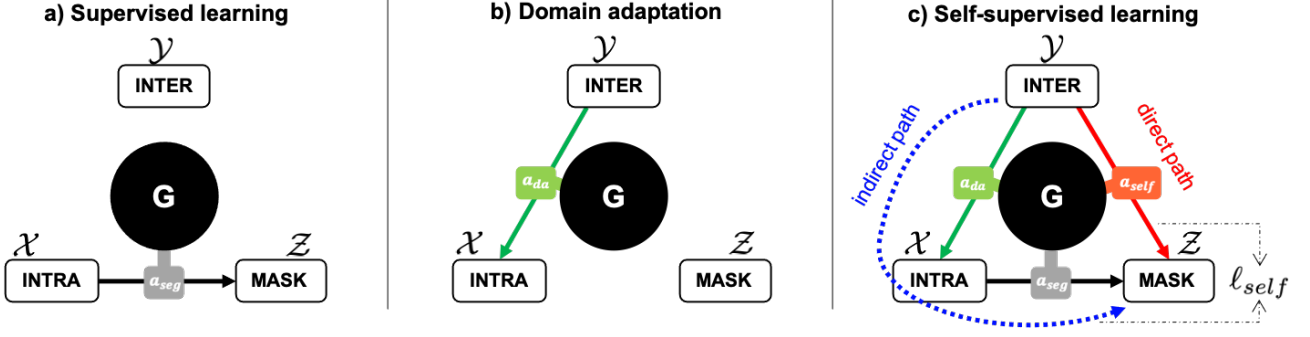


Fig. 1. Overview of the unified domain adaptation and segmentation framework. A single generator  $G$  can transfer domains by simply using task-specific AdaIN codes  $a_{seg}$ ,  $a_{da}$  and  $a_{self}$  for segmentation, domain adaptation and self-supervised learning task, respectively.

#### 2.4. Self-supervised learning

Recent emerging researches on self-supervised learning has brought large improvements in medical domain adaptation or image segmentation tasks, by promoting consistency between model outputs given a same input with different perturbations or by training an auxiliary proxy task (Xue et al., 2020; Orbes-Arteaga et al., 2019; Li et al., 2020b). In general, DL models trained with auxiliary self-supervised losses are proven to achieve better generalization capability as well as better primary task performance, especially when training with limited labeled dataset and abundant unlabeled dataset.

For examples, (Xue et al., 2020) achieved SOTA performance on cross-modality domain adaptation aided by self-supervised learning, by constructing an auxiliary edge generation task to leverage unlabeled domain dataset. (Orbes-Arteaga et al., 2019) and (Li et al., 2020b) introduced a consistency loss between outputs between a student and a teacher model, given unlabeled input with different augmentation.

### 3. The Proposed Framework

#### 3.1. Key idea

One of the unique features of StarGANv2 (Choi et al., 2020) image translation approach is that it can synergistically learn common features over multiple domains via shared layers of networks to fully leverage all the training datasets, but still enables the domain specific adaption using different AdaIN codes. Inspired by this, our network is designed to unify the domain adaptation and segmentation via AdaIN-based knowledge distillation.

Specifically, our framework categorizes the training data into three distinct groups: the segmentation mask [MASK], and their matched input image domain [INTRA], and domain-shifted input images with no segmentation labels [INTER]. More specifically, the training data in the [INTRA] domain have matched segmentation mask in the [MASK] domain, whereas large number of training dataset in [INTER] domain do not have segmentation masks (see Fig. 1).

Due to the domain shift between [INTRA] and [INTER] domains, the trained network in a supervised manner using [INTRA] data does not generalize well for the [INTER] domain images. To mitigate this problem, our key idea is that a single

generator trained along with the adaptive instance normalization (AdaIN) can perform supervised segmentation using [INTRA] data for a specific AdaIN code (see Fig. 1(a)) as well as the domain adaptation between [INTER] and [INTRA] domains using another AdaIN code (see Fig. 1(b)). The network is then trained in a self-supervised manner that enforces the direct segmentation results to be consistent with the another segmentation results through domain adaptation followed by segmentation, so that a direct segmentation using [INTER] images can be done by using yet another AdaIN code (see Fig. 1(c)). This enables the knowledge distillation between various tasks.

Once the networks are trained, only a single generator and pre-built AdaIN codes can be simply used at the inference phase for both [INTRA] and [INTER] domain image segmentation, which makes the proposed method more practical.

#### 3.2. Overall framework

Inspired by StarGANv2 (Choi et al., 2020), the overall architecture of our network is shown in Fig. 2, which is composed of a single generator  $G$ , a style encoder  $S$ , AdaIN code generators for the encoder and decoder,  $F_e$  and  $F_d$ , respectively, and a multi-head discriminator  $D$ . One of the reasons StyleGANv2 introduced the style encoder  $S$  is to impose additional constraint in the AdaIN code generation so that the AdaIN code generator can be regularized to generate meaningful codes (Choi et al., 2020). Here, the style encoder, AdaIN code generators, and discriminators have multi-head structure, as will be explained later.

One of the key differences of our network from StarGANv2 is an encoder-decoder architecture that has independent AdaIN code layers for encoder and decoder. Because of the two separate AdaIN codes for encoder and decoder, the proposed generator can perform either supervised segmentation, domain adaptation and self-supervised learning, by simply changing the combination of the AdaIN codes from the two AdaIN code generators as shown in Table 1.

For example, for the segmentation task, the constant AdaIN code (0, 1) is used for both encoder and decoder, leading to the standard instance normalization (Ulyanov et al., 2016). On the other hand, learnable AdaIN codes are used for decoder AdaIN layers in the translation toward [INTRA] and [INTER] domains. Yet another learnable AdaIN codes are used for en-

coder AdaIN layer for self-supervised learning task to enforce consistent reconstruction from various paths.

Specifically, let  $\mathcal{X}$ ,  $\mathcal{Y}$  and  $\mathcal{Z}$  refer to the [INTRA], [INTER] and [MASK] domains associated with the probability distribution  $P_X$ ,  $P_Y$  and  $P_Z$ . Then, our generator is defined by

$$v = G(u, a), \quad a := (F_e, F_d) \quad (1)$$

where  $u$  is the input image either in  $\mathcal{X}$  or  $\mathcal{Y}$ ,  $a \in \{a_{seg}, a'_{seg}, a_{da}^X, a_{da}^Y, a_{self}\}$  refers to the AdaIN code as shown in Table 1. Depending on the input data and AdaIN codes, the network output  $v$  can be either in  $\mathcal{X}$ ,  $\mathcal{Y}$ , or  $\mathcal{Z}$ . In the following, we provide more detailed description how this network can be trained.

**Table 1. AdaIN codes combination for various training tasks.**

AdaIN codes	Task	$F_e$ (mean, std)	$F_d$ (mean, std)	Training type
$a_{seg}$	[INTRA] $\rightarrow$ [MASK]	(0, 1)	(0, 1)	segmentation
$a'_{seg}$	[INTRA] $\rightarrow$ [MASK]	(0, 1)	learnable	dummy segmentation code
$a_{da}^X$	[INTER] $\rightarrow$ [INTRA]	(0, 1)	learnable	domain adaptation
$a_{da}^Y$	[INTRA] $\rightarrow$ [INTER]	(0, 1)	learnable	domain adaptation
$a_{self}$	[INTER] $\rightarrow$ [MASK]	learnable	(0, 1)	self-supervised

### 3.3. Neural network training

Our training losses are extended from those of StarGANv2 (Choi et al., 2020), with specific modification to include the segmentation tasks and self-supervised learning. The details are as follows.

#### 3.3.1. Supervised segmentation

This part is unique contribution of our work compared to StarGANv2. Fig. 1(a) shows the supervised segmentation, which can be considered as conversion from [INTRA] to [MASK] domain. In this case, the generator is trained by the following:

$$\min_{G,S} \lambda_{seg} \ell_{seg}(G) + \lambda_{style} \ell_{style}(G, S), \quad (2)$$

where  $\lambda_{seg}$  and  $\lambda_{style}$  are hyper-parameters, and the segmentation loss  $\ell_{seg}$  is defined by the cross-entropy loss between generated output and its matched label:

$$\ell_{seg}(G) = -\mathbb{E} \left[ z_i \log \hat{p}_i(G(x, a_{seg})) \right], \quad (3)$$

where  $z_i$  denotes the  $i$ -th pixel of the ground truth segmentation mask  $z \in \mathcal{Z}$  with respect to the input image  $x \in \mathcal{X}$ ,  $\hat{p}_i(G)$  denotes the softmax probability function of the  $i$ -th pixel in the generated fake image by  $G(x, a_{seg})$ .

Once a segmentation result is generated for a given AdaIN style code, the style encoder that has the segmentation result as an input is enforced to be consistent with dummy AdaIN code  $a'_{seg}$  that is generated from the style encoder for the [MASK] domain. This can be achieved by using the following style loss:

$$\ell_{style}(G, S) = \mathbb{E}_{x \sim P_X} \left[ \|a'_{seg} - S(G(x, a_{seg}))\|_1 \right], \quad (4)$$

where  $a'_{seg}$  denotes an [MASK] domain-specific AdaIN code. Although this code is not used for segmentation directly, the

generation of this AdaIN code from the style coder or the AdaIN code generator turns out to be important to train the shared layer in the multi-head structure of the AdaIN code generator and the style encoder (see Figs. 3(b)(c)). This issue will be discussed in detail later.

#### 3.3.2. Domain adaptation

The training of domain adaptation is basically similar to StarGANv2. Fig. 1(b) shows the training scheme for the domain adaptation between  $\mathcal{X}$  and  $\mathcal{Y}$ . We train the proposed network by solving the following optimization problem:

$$\min_{G,S,F_e,F_d} \max_D \ell_{da}(G, F_e, F_d, S, D), \quad (5)$$

where the domain adaptation loss is given by

$$\begin{aligned} \ell_{da}(G, F_e, F_d, S, D) = & \ell_{adv}(G, D, F_d, S) \\ & + \lambda_{cycle} \ell_{cycle}(G, S) \\ & + \lambda_{style} \ell_{style}(G, S) \\ & - \lambda_{div} \ell_{div}(G, F_d, S), \end{aligned}$$

where  $\lambda_{cycle}$ ,  $\lambda_{style}$  and  $\lambda_{div}$  are hyper-parameters and  $\ell_{adv}$  is the adversarial loss defined by

$$\begin{aligned} \ell_{adv}(G, D, F_d, S) = & \mathbb{E}_{s \sim P_S} [\log D_S(s)] + \mathbb{E}_{s \sim P_S} [\log(1 - D_{\mathcal{T}}(G(s, a_{da}^{\mathcal{T}})))] \end{aligned} \quad (6)$$

where the domains  $\mathcal{S}$  and  $\mathcal{T}$  are source and target domains, which are chosen randomly from  $\mathcal{X}$  and  $\mathcal{Y}$  so that (6) can consider all the combinations of source and target domains so that different headers of the discriminator can be optimized for each  $\mathcal{X}$  or  $\mathcal{Y}$  domain (see Fig. 3(a)). Furthermore, the learnable part of the AdaIN code  $a_{da}^{\mathcal{T}}$  is generated either from the encoder AdaIN coder generator  $F_d$  or from the style encoder  $S(x)$  given a reference target  $t \in \mathcal{T}$  (see Fig. 3(b)(c)) so that their headers can be optimized as well. This technique was successfully used in StarGANv2, so we followed the same procedure.

Using similar random choices of source and target domain, we define the cycle-consistency loss  $\ell_{cycle}$  as follows:

$$\ell_{cycle}(G, S) = \mathbb{E}_{s \sim P_S} \left[ \|x - G(G(s, a_{da}^{\mathcal{T}}), a_{da}^{\mathcal{S}})\|_1 \right]. \quad (7)$$

Similar to the cycle-consistency loss  $\ell_{cycle}$  for the images, we introduce the style loss  $\ell_{style}$  in (4) to enforce the cycle-consistency in the AdaIN code domain. More specifically, once a fake image is generated using a domain-specific AdaIN code, the style encoder with the fake image as an input should reproduce the original AdaIN code. This can be achieved by using the following style loss:

$$\ell_{style}(G, S) = \mathbb{E}_{s \sim P_S} \left[ \|a_{da}^{\mathcal{T}} - S(G(s, a_{da}^{\mathcal{T}}))\|_1 \right]. \quad (8)$$

Finally, to make the generated fake images diverse, the difference between two fake images that are generated by two different AdaIN codes should be maximized. This can be achieved

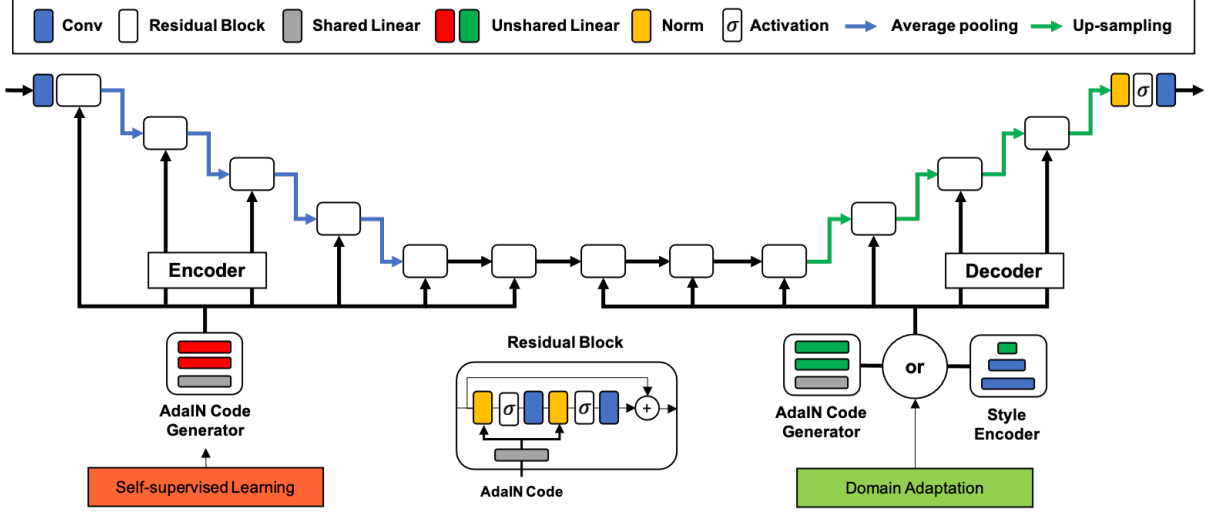


Fig. 2. The overall architecture of the generator connected to two AdaIN code generators and a style encoder. The generator is divided into an encoder and a decoder which are composed of series of residual blocks. The output codes generated from either AdaIN code generators or the style encoder are connected to AdaIN layers of each residual blocks.

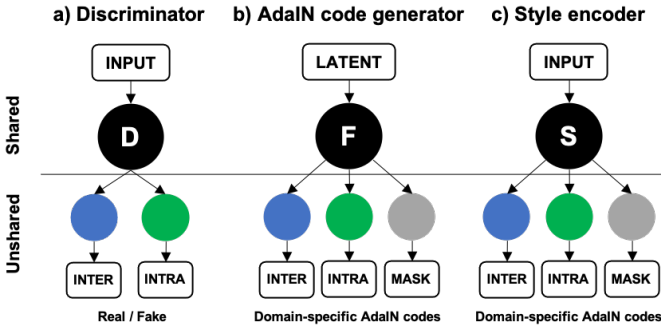


Fig. 3. The architecture of multi-headed discriminator, AdaIN code generator and style encoder. Each network is composed of a shared module followed by domain-specific unshared layers.

by maximizing the following loss:

$$\ell_{div}(G, F_d, S) = \mathbb{E}_{s \sim P_S} [\|G(s, a_{da}^T) - G(s, a_{self}^T)\|_1], \quad (9)$$

where  $a_{da}^T$  and  $a_{self}^T$  can be randomly generated from the AdaIN code generator, or from the style encoder  $S$  given two different images.

### 3.3.3. Self-supervised learning

This part is another unique contribution of our work compared to StarGANv2. The goal of the self-supervised learning is that the image in [INTER] domain can directly generate the segmentation results, as described as red arrow in Fig. 1(c).

Specifically, since [INTER] domain lacks segmentation mask, knowledge learned from both the supervised learning and domain adaptation need to be distilled. Thus, our contribution comes from introducing novel constraints: a segmentation output trained in a self-supervised manner should be consistent with another segmentation output generated through the domain adaptation followed by supervised segmentation, as described as green and black arrows, respectively, in Fig. 1(c).

In addition, at the inference phase, it is often difficult to know which domain the input comes from. Therefore, one AdaIN code should deal with both [INTRA] and [INTER] domain image segmentation. This leads to the following self-consistency loss:

$$\ell_{self}(G, F_e) \quad (10)$$

$$= \lambda_{inter} \ell_{inter}(G, F_e) + \lambda_{intra} \ell_{intra}(G, F_e) \quad (11)$$

$$= \mathbb{E}_{y \sim P_Y} [\|G(y, a_{da}^T) - G(y, a_{self}^T)\|_1] \quad (12)$$

$$+ \mathbb{E}_{x \sim P_X} [\|G(x, a_{self}^T) - G(x, a_{seg})\|_1], \quad (13)$$

where  $\ell_{inter}$  and  $\ell_{intra}$  denote inter-domain and intra-domain self-consistency loss, respectively, and  $\lambda_{inter}$  and  $\lambda_{intra}$  are hyper-parameters for each.

In fact, this procedure can be regarded as teacher-student approach. The indirect path in Fig. 1(c) is a teacher network that guides the training procedure of the student network in the direct path in Fig. 1(c). In contrast to the existing teacher-student approaches (Tarvainen and Valpola, 2017; Li et al., 2020a; Perone et al., 2019), our approach however does not need separate networks for the teacher and student: instead, the same generator with different AdaIN combinations serves as teacher or student, which is another big advantage of our method.

In order to train our single generator framework for the self-supervised learning tasks without sacrificing the supervised segmentation performance, we introduce AdaIN code generator  $F_e$  to the encoder, whereas the decoder still uses the fixed AdaIN code (1, 0) (see Table 1) which corresponds to the standard instance normalization.

## 4. Methods

### 4.1. Network architecture

Our generator  $G$  is composed of encoder and decoder modules. Specifically, the encoder part is composed of four down-sampling residual blocks and two intermediate residual blocks.

The decoder part is composed of two intermediate residual blocks and four up-sampling residual blocks. Each residual block is composed of AdaIN layers, activation layers, and convolution layers, respectively. All the AdaIN layers are connected to the AdaIN code generator, and for the decoder module, the style encoder is also connected for domain adaptation task.

Similar to StarGANv2, our discriminator  $D$  is composed of shared convolution layers followed by multi-headed unshared convolution layers for each image domain, i.e., [INTER], [INTRA], as shown in Fig. 3(a). In the discriminator, the input images can be classified to 1 or 0 for each domain separately, where 1 indicates real and 0 indicates fake. The AdaIN code generator is composed of shared linear layers followed by multi-headed unshared linear layers for each domain, as shown in Fig. 3(b). Thus, AdaIN codes for each domain can be generated via the shared layer followed by domain-specific unshared layers, respectively. In addition, the style encoder is composed of shared convolution layers followed by multi-headed unshared linear layers for each domain, as shown in Fig. 3(c). In the style encoder, input images can be decoded into domain-specific AdaIN codes for each domain through both shared and unshared layers.

Thanks to the existence of the shared layer, the knowledge from a specific domain translation can be distilled to the other domains, improving overall performance of discriminator, AdaIN code generator, and style encoder (Choi et al., 2020).

Detailed specification of each network is provided in Appendix A.

#### 4.2. Dataset

To evaluate the performance of proposed domain adaptation and segmentation tasks, we utilized public CXR datasets. For the supervised segmentation task, normal CXR images in JSRT dataset (Shiraishi et al., 2000) with its paired lung annotations from SCR dataset (Van Ginneken et al., 2006) are used as [INTRA] and [MASK] domains, respectively. As for abnormal CXR images (i.e. [INTER] domain), we collected pneumonia CXR dataset from four different sources, e.g., RSNA COVID-19 dataset (Desai et al., 2020), Cohen pneumonia dataset (Cohen et al., 2020), BRISIA COVID-19 dataset (Borghesi and Maroldi, 2020), and BIMCV dataset (de la Iglesia Vayá et al., 2020), whose characteristics are described in Table 2.

#### 4.3. Implementation details

The proposed network was trained by feeding input images from a pair of two randomly chosen domains, one for the source domain and the other for the target domain. For example, if a domain pair composed of [INTER] and [INTRA] domains is fed into the network, the network is trained for the domain adaptation task. When a domain pair, composed of [INTRA] as source and [MASK] as target domain, is fed into the network, the network is trained for the supervised segmentation task. For self-supervised learning, an image from [INTER] domain is fed as the source domain to output the segmentation mask in [MASK] domain, as well as from [INTRA] to [MASK] domain. In terms of the training sequence, the self-supervised training

starts after the supervised segmentation and domain adaptation tasks are performed.

The proposed method was implemented with PyTorch library (Paszke et al., 2017). We applied Adam optimizer (Kingma and Ba, 2014) to train the models and set the batch size 1. The model was trained using a NVIDIA GeForce GTX 1080 Ti GPU. Hyper parameters were chosen to be  $\lambda_{cycle} = 2$ ,  $\lambda_{style} = 1$ ,  $\lambda_{div} = 1$ ,  $\lambda_{seg} = 5$ ,  $\lambda_{inter} = 10$  and  $\lambda_{intra} = 1$ . Learning rate was optimized to 0.0001.

All the input CXR images and labels are resized to  $256 \times 256$ . We did not perform any pre-processing or data augmentation except for normalization of pixel intensity to  $[-1, 0, 1.0]$ . The network was trained for 20K iterations to simultaneously train domain adaptation and supervised segmentation tasks. We adopted early stopping strategy based on validation performance of supervised segmentation task. After training the segmentation and the domain adaptation tasks until they guarantee certain performances, the network was continued to be trained in self-supervised manner for additional 5K iterations. Once training iteration reaches certain fixed iteration points throughout the total iterations, the learning rate was reduced by factor 10.

#### 4.4. Comparative methods

For the domain adaptation task, we used MUNIT (Huang et al., 2018) and the original StarGANv2 as baseline models for comparative studies, and trained the models with [INTRA] and [INTER] domain images with same experimental setting to those of the propose model. For the segmentation task, we use U-Net (Ronneberger et al., 2015) as a baseline, and trained with same experimental setting to that of the proposed segmentation task. To compare the synergetic effect of domain adaptation and segmentation tasks, we added XLSor (Tang et al., 2019) as an additional baseline. XLSor is tested by utilizing pre-trained weight provided by the author, which was trained in a semi-supervised manner with massively generated pseudo-labeled pneumonia dataset via MUNIT (Huang et al., 2018).

At the inference phase, as post-processing steps for the segmentation task, two largest contours were automatically selected based on contour areas, and any holes within each contour are filled. The same postprocessing step is applied for all methods for fair comparison.

#### 4.5. Evaluation

For the CXR dataset, segmentation performance with respect to unseen normal CXR data with ground-truth segmentation masks was quantified using dice similarity score (Dice) index of both lung contours.

On the other hand, due to the lack of ground-truth label, the domain adaptation and self-supervised segmentation performance of [INTER] domain were evaluated based on generation of expected lung structure covered with highly-consolidated regions. Rectangular boxes, which fully cover each lung structure, was manually drawn on CXR images. Then, the degree of fitness was qualitatively evaluated on generated fake images and segmentation results.



Table 2. Chest X-ray dataset resources.

	Dataset	Nation	Disease class	bit	View	Total	Training	Val	Test	
									internal	external
Supervised train set	JSRT / SCR	Japan	Normal, Nodule	12	PA	247	178	20	49	-
	RSNA	USA	Pneumonia (COVID-19)	10	AP	218	218	-	-	-
Unsupervised train set	Cohen et al.	-	Pneumonia (COVID-19, Virus, Bacteria, Tuberculosis)	8	PA, AP	680	640	-	40	-
Test dataset	BRIXIA	Italy	Pneumonia (COVID-19)	16	AP	2384	-	-	-	2384
	BIMCV	Spain	Pneumonia (COVID-19)	16	AP	374	-	-	-	374

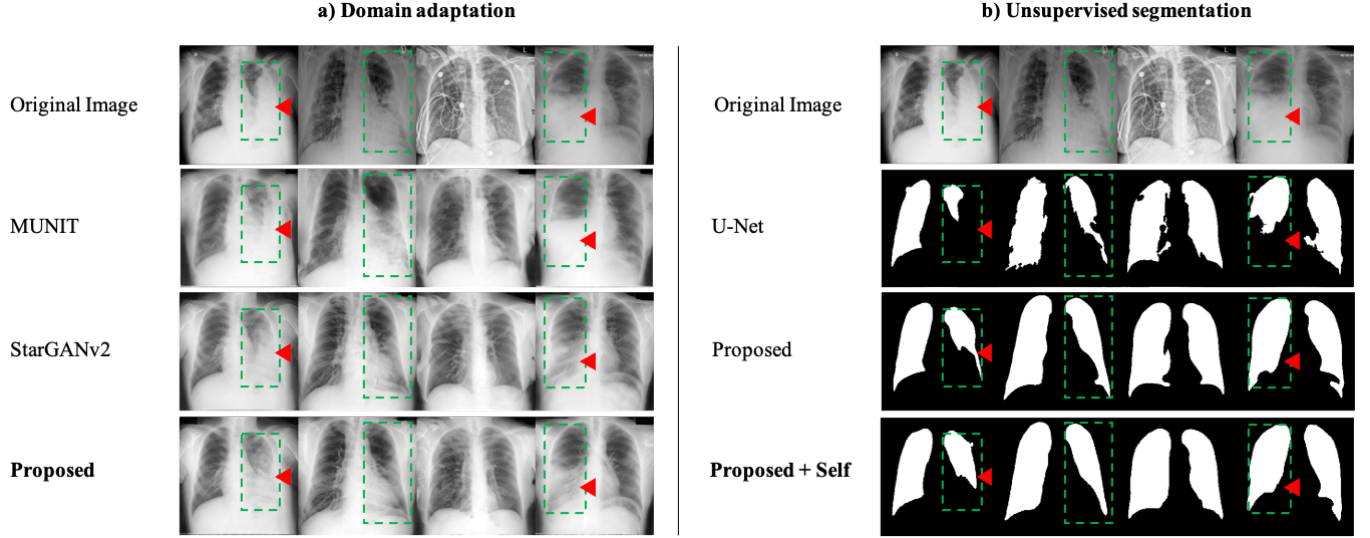


Fig. 4. Domain adaptation and segmentation results comparison using the internal test set. Green dashed boxes indicate expected lung regions.

## 5. Experimental Results

### 5.1. Domain adaptation

Fig. 4(a) shows the domain adaptation performance from abnormal CXR to normal CXR. Compared to the MUNIT and the original StarGANv2, the proposed method shows superior domain adaptation performance from pneumonia lung to normal lung. Note that the proposed method is the only one method that successfully transfer highly consolidated region as like normal lung, as illustrated in red triangles in the fourth row of Fig. 4(a).

### 5.2. Unsupervised segmentation

Fig. 4(b) shows unsupervised segmentation performance of abnormal CXR domain images. Compared to the baseline model without domain adaptation, the proposed methods successfully segment lung structure in pneumonia CXR images, which is covered with extremely consolidated regions, indicated as red triangles in the 1st and 4th columns of Fig. 4(b). In particular, the proposed model trained with self-consistency loss shows most promising segmentation performance, showing that the segmentation results perfectly fit in the expected lung area, as illustrated as green dashed boxes in the 4th row of Fig. 4(b).

Fig. 5 compares unsupervised segmentation performance on unseen external test dataset. External test dataset, composed of

two COVID-19 pneumonia database, have various intensity distribution as depicted in Fig. 5(a). The U-Net mostly fail to segment regular lung shapes from pneumonia lungs, which shows way-shifted intensity distribution from that of source domain as depicted in Fig. 5(b). The XLSor shows promising segmentation performance on mild-opacity pneumonia cases (See the 4th and the 12th columns of Fig. 5(c)), whereas, for severe cases of pneumonia, the XLSor under-segments part of lung area or fails to be generalized on domain-shifted inputs (See the 1st, 5th and 10th columns of of Fig. 5(c)). The proposed methods show most promising segmentation performance on unseen dataset. In Fig. 5(d-e), the proposed method successfully segmented lung structures in domain-shifted inputs without under-segmentation or severe over-segmentation. Moreover, segmentation results generated by the proposed model trained with self-consistency loss, show better fitness to the expected lung regions compared to the proposed method without self-supervised learning.

To verify that the proposed methods can still retain the supervised segmentation performance for normal CXR images, we compare the segmentation performance on test dataset composed of normal CXR images using other networks. Table 3 presents Dice indices of lung segmentation results. Compared to both the U-Net and the XLSor of Dice index 0.976, which is currently SOTA performance of deep-learning based normal lung segmentation (Jangam and Rao, 2018), the proposed methods showed comparable Dice index in addition to providing su-

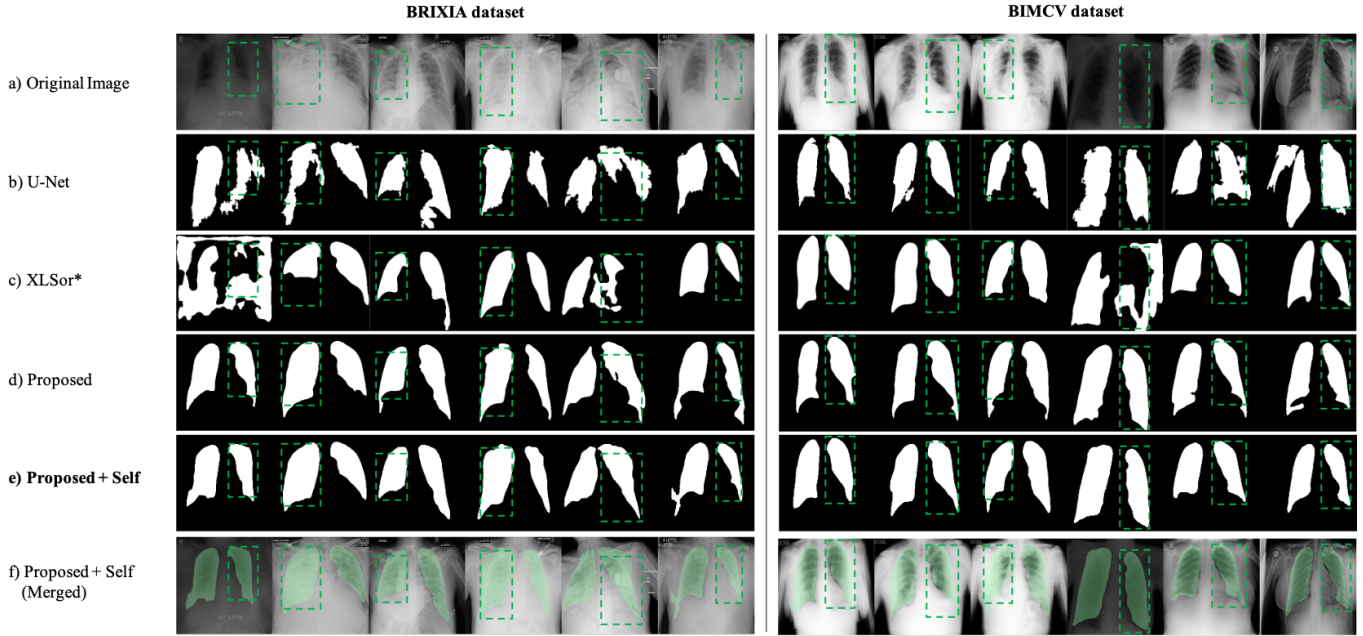


Fig. 5. Unsupervised segmentation results comparison using the external test set. Green dashed boxes indicate expected lung regions. The asterisk (\*) indicates results generated with pre-trained model weight provided by authors.

perb performance for the abnormal CXR.

Table 3. Segmentation performance of chest X-ray dataset.

Method	Normal CXR	Abnormal CXR
	Dice index	Qualitative evaluation
U-Net	<b>0.976</b> $\pm$ 0.012	Fig. 5b
XLSor*	<b>0.976</b> $\pm$ 0.010	Fig. 5c
Proposed	0.966 $\pm$ 0.013	Fig. 5d
Proposed + Self	0.959 $\pm$ 0.014	<b>Fig. 5e</b>

The asterisk (\*) indicates performance reported.

### 5.3. Computational costs

The proposed unified framework costs less training computation resources, compared to training individual domain adaptation and segmentation networks. Table 4 shows total network parameters of each methods, based on training CXR dataset. Once the model is trained, only the generator with pre-built AdaIN codes are used at the inference phase, thus the model costs only the single generator.

## 6. Discussion

### 6.1. Ablation study

We analyzed contribution of each loss for the segmentation task. We cumulatively added each component to the baseline model, which is trained with domain adaptation losses-only, and evaluated supervised segmentation performance on normal CXR. Table 5 presents Dice indices of lung segmentation result. There were no significant differences among different configurations.

Table 4. Number of trainable parameters in various networks for segmentation and domain adaptation.

Method	Network parameters		
	Generator	Others	Total
<b>Segmentation-only</b>			
U-Net	29M	-	29M
XLSor	67M	-	67M
<b>Domain adaptation-only</b>			
MUNIT	30M	17M	47M
<b>Segmentation + Domain adaptation</b>			
XLSor + MUNIT			114M
Proposed	34M	45M	79M

Then, domain adaptation and unsupervised segmentation performance on abnormal CXR were qualitatively evaluated. Fig. 6 presents performances of each configuration on both the internal and external test set. In configuration (b) with additional segmentation loss, domain adaptation performance was superior to the baseline. However, we observe that the segmentation results have several concave regions as depicted in 2nd and 4th columns of Fig. 6(b), which fail to resemble the general shape of lung structure. In configuration (c) with additional style loss, segmentation results resemble normal lung better than (b), thanks to the style loss, which can extract common features of normal and abnormal CXR via the shared layer of the style encoder. In configuration (d) with additional cycle-consistency loss, we observed rather degraded lung segmentation performance as depicted in 2nd and 4th columns of Fig. 6(d), which have more concave regions compared to that of (c). The cycle-consistency loss, which try to revert the generated lung mask back to the original image, disturbs the network to generate lung segments on extremely consolidated lung regions.



Based on this ablation study, we set the configuration (c), which trained with the segmentation loss and the style loss, as our proposed method for supervised segmentation task (see Equation 2).

**Table 5. Analysis of the segmentation components.**

Method	Segmentation components	Normal CXR Dice index
a) Baseline	-	-
b) + Segmentation loss	$\ell_{seg}$	$0.965 \pm 0.013$
c) + Style loss	$\ell_{seg} + \ell_{style}$	<b><math>0.966 \pm 0.013</math></b>
d) + Cycle loss	$\ell_{seg} + \ell_{style} + \ell_{cycle}$	<b><math>0.966 \pm 0.013</math></b>

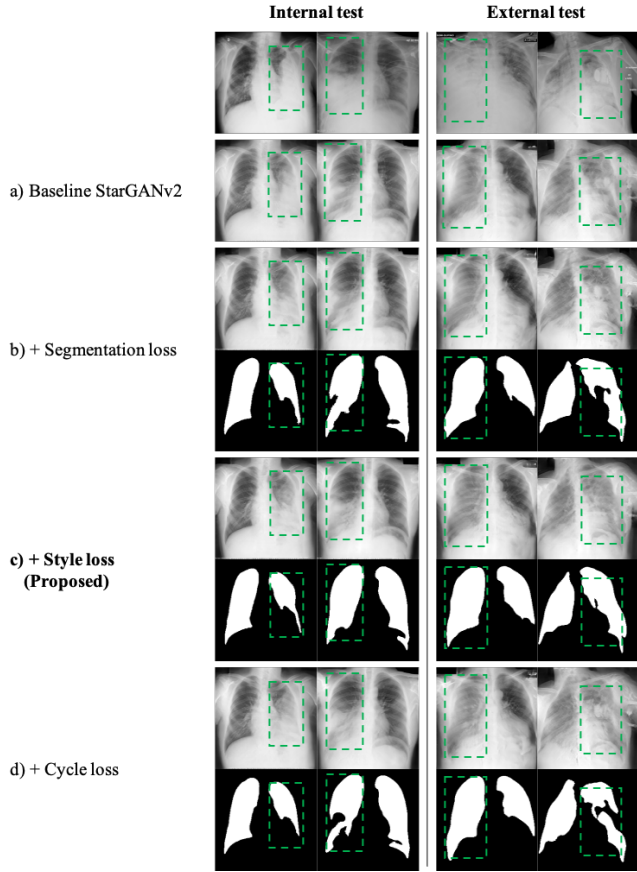


**Fig. 6. Component analysis of segmentation task using the internal and external test set. Green dashed boxes indicate expected lung regions.**

### 6.2. Abnormal lung segmentation on chest X-ray dataset

Our model provides promising unsupervised segmentation performance, by extracting common features from normal and abnormal CXR dataset, thanks to the shared modules of each network components. Moreover, the model can be trained with both domain adaptation and segmentation tasks within a single generator, thus, the model can fully leverage knowledge distilled from both supervised learning tasks.

Even with the pneumonia CXR images, which are usually covered with high-opacity lung region, our method can provide successful segmentation results similar to normal CXR. In

particular, the model trained with self-supervised learning provides more realistic lung segmentation results, which actually reflect expected lung regions of the original CXR images. Self-supervised learning can minimize artifacts induced by performing segmentation of fake images (transferred from abnormal to normal style), and directly transfer original abnormal CXR images to label outputs, more efficiently.

Specifically, our model outperforms other methods when testing on external COVID-19 CXR datasets, despite there exist large domain shifts from trained dataset (Fig. 5). The generalization performance can be achieved thanks to regularization effect induced by learning domain-invariant features via shared components.

## 7. Conclusions

We presents a unified framework for domain adaptation, supervised segmentation and self-supervised segmentation tasks using AdaIN based knowledge distillation that performs various task by simply changing task-specific AdaIN codes. The proposed network can synergistically learn common features from different domains and different tasks using a single generator. Our results demonstrate that the proposed framework successfully perform knowledge distillation from supervised tasks, and provide SOTA performance for the unsupervised pneumonia CXR segmentation task.

## 8. Acknowledgement

This work was supported by grant No. MCM-2021-N11210024 from KAIST Mobile Clinic Module Project.

## Appendix A. Network Architecture

We provide details of the proposed framework, which consists of four sub-networks, shown in Table A.6, A.7, A.8 and A.9.

Note that input for the domain adaption is a single channel image, whereas the domain adaption from segmentation masks requires two channel to separate foreground and background. Accordingly, the input and output with different channel sizes of  $C_{da}$  and  $C_{seg}$ , for each domain adaptation and segmentation tasks, can be processed in each unified network via unshared modules.

## References

- Bai, W., Oktay, O., Sinclair, M., Suzuki, H., Rajchl, M., Tarroni, G., Glocker, B., King, A., Matthews, P.M., Rueckert, D., 2017. Semi-supervised learning for network-based cardiac mr image segmentation, in: International Conference on Medical Image Computing and Computer-Assisted Intervention, Springer. pp. 253–260.
- Borghesi, A., Maroldi, R., 2020. Covid-19 outbreak in italy: experimental chest x-ray scoring system for quantifying and monitoring disease progression. *La radiologia medica* 125, 509–513.
- Chen, C., Dou, Q., Chen, H., Qin, J., Heng, P.A., 2020. Unsupervised bidirectional cross-modality adaptation via deeply synergistic image and feature alignment for medical image segmentation. *IEEE transactions on medical imaging* 39, 2494–2505.

**Table A.6. Generator network architecture.**

Module	Layer	Norm	Resample	Input dimension (C × H × W)
In	Conv 1×1	-	-	$C_{da} \times 256 \times 256$
Encoder	ResBlock × 4	AdaIN	Down	$64 \times 256 \times 256$
	ResBlock × 2	AdaIN	-	$512 \times 16 \times 16$
Decoder	ResBlock × 2	AdaIN	-	$512 \times 16 \times 16$
	ResBlock × 4	AdaIN	Up	$512 \times 16 \times 16$
Unshared	Norm	IN	-	
	Leaky ReLU	-	-	$64 \times 256 \times 256$
	Conv 1×1	-	-	
Output				$C_{da} \times 256 \times 256$
				$C_{seg} \times 256 \times 256$

**Table A.7. AdaIN code generator architecture.**

Type	Layer	Input dimension (C)
In	Latent z	4
Shared	Linear × 3	4
	Linear × 1	512
Unshared	Linear × 3	512
	Linear × 1	512
Output	-	$16 \times K$

**Table A.8. Style encoder architecture.**

Type	Layer	Input channel (C)	Input size (H × W)
Unshared	Conv 1×1	$C_{da}, C_{seg}$	$256 \times 256$
	ResBlock × 6	64	$256 \times 256$
Shared	Leaky ReLU	512	$4 \times 4$
	Conv 4×4	512	$4 \times 4$
	Leaky ReLU	512	$1 \times 1$
Unshared	Linear	512	$1 \times 1$
Output	-	$16 \times K$	-

**Table A.9. Discriminator architecture.**

Type	Layer	Input channel ( $C_{da}$ )	Input size (H × W)
Shared	Conv 1×1	1	$256 \times 256$
	ResBlock × 6	64	$256 \times 256$
	Leaky ReLU	512	$4 \times 4$
	Conv 4×4	512	$4 \times 4$
	Leaky ReLU	512	$1 \times 1$
Unshared	Conv 1×1	512	$1 \times 1$
Output	-	$1 \times K$	-

Choi, Y., Uh, Y., Yoo, J., Ha, J.W., 2020. Stargan v2: Diverse image synthesis for multiple domains, in: Proceedings of the IEEE/CVF Conference on Computer Vision and Pattern Recognition, pp. 8188–8197.

Cohen, J.P., Morrison, P., Dao, L., 2020. COVID-19 image data collection. arXiv 2003.11597 URL: <https://github.com/ieee8023/covid-chestxray-dataset>.

De Fauw, J., Ledsam, J.R., Romera-Paredes, B., Nikolov, S., Tomasev, N., Blackwell, S., Askham, H., Glorot, X., O'Donoghue, B., Visentin, D., et al., 2018. Clinically applicable deep learning for diagnosis and referral in retinal

disease. *Nature medicine* 24, 1342–1350.

Desai, S., Baghal, A., Wongsurawat, T., Jenjaroenpun, P., Powell, T., Al-Shukri, S., Gates, K., Farmer, P., Rutherford, M., Blake, G., et al., 2020. Chest imaging representing a covid-19 positive rural us population. *Scientific data* 7, 1–6.

Huang, X., Belongie, S., 2017. Arbitrary style transfer in real-time with adaptive instance normalization, in: Proceedings of the IEEE International Conference on Computer Vision, pp. 1501–1510.

Huang, X., Liu, M.Y., Belongie, S., Kautz, J., 2018. Multimodal unsupervised image-to-image translation, in: Proceedings of the European conference on computer vision (ECCV), pp. 172–189.

de la Iglesia Vayá, M., Saborit, J.M., Montell, J.A., Pertusa, A., Bustos, A., Cazorla, M., Galant, J., Barber, X., Orozco-Beltrán, D., García-García, F., Caparrós, M., González, G., Salinas, J.M., 2020. Bimcv covid-19+: a large annotated dataset of rx and ct images from covid-19 patients. arXiv:2006.01174.

Jangam, E., Rao, A., 2018. Public datasets and techniques for segmentation of anatomical structures from chest x-rays: Comparative study, current trends and future directions, in: International Conference on Recent Trends in Image Processing and Pattern Recognition, Springer. pp. 321–331.

Kingma, D.P., Ba, J., 2014. Adam: A method for stochastic optimization. arXiv preprint arXiv:1412.6980.

Li, K., Wang, S., Yu, L., Heng, P.A., 2020a. Dual-teacher: Integrating intra-domain and inter-domain teachers for annotation-efficient cardiac segmentation, in: International Conference on Medical Image Computing and Computer-Assisted Intervention, Springer. pp. 418–427.

Li, X., Yu, L., Chen, H., Fu, C.W., Xing, L., Heng, P.A., 2020b. Transformation-consistent self-ensembling model for semisupervised medical image segmentation. *IEEE Transactions on Neural Networks and Learning Systems*.

Oh, Y., Park, S., Ye, J.C., 2020. Deep learning covid-19 features on cxr using limited training data sets. *IEEE Transactions on Medical Imaging* 39, 2688–2700. doi:10.1109/TMI.2020.2993291.

Orbes-Arteaga, M., Varsavsky, T., Sudre, C.H., Eaton-Rosen, Z., Haddow, L.J., Sørensen, L., Nielsen, M., Pai, A., Ourselin, S., Modat, M., et al., 2019. Multi-domain adaptation in brain mri through paired consistency and adversarial learning, in: Domain Adaptation and Representation Transfer and Medical Image Learning with Less Labels and Imperfect Data. Springer, pp. 54–62.

Ouyang, X., Huo, J., Xia, L., Shan, F., Liu, J., Mo, Z., Yan, F., Ding, Z., Yang, Q., Song, B., et al., 2020. Dual-sampling attention network for diagnosis of covid-19 from community acquired pneumonia. *IEEE Transactions on Medical Imaging* 39, 2595–2605.

Paszke, A., Gross, S., Chintala, S., Chanan, G., Yang, E., DeVito, Z., Lin, Z., Desmaison, A., Antiga, L., Lerer, A., 2017. Automatic differentiation in PyTorch, in: NIPS Autodiff Workshop.

Perone, C.S., Ballester, P., Barros, R.C., Cohen-Adad, J., 2019. Unsupervised domain adaptation for medical imaging segmentation with self-ensembling. *NeuroImage* 194, 1–11.

Ronneberger, O., Fischer, P., Brox, T., 2015. U-net: Convolutional networks for biomedical image segmentation, in: International Conference on Medical image computing and computer-assisted intervention, Springer. pp. 234–241.

Shiraishi, J., Katsuragawa, S., Ikezoe, J., Matsumoto, T., Kobayashi, T., Komatsu, K.I., Matsui, M., Fujita, H., Kodera, Y., Doi, K., 2000. Development of a digital image database for chest radiographs with and without a lung nodule. *American Journal of Roentgenology* 174, 71–74. URL: <https://doi.org/10.2214/ajr.174.1.1740071>, doi:10.2214/ajr.174.1.1740071.

Tang, Y.B., Tang, Y.X., Xiao, J., Summers, R.M., 2019. Xlsor: A robust and accurate lung segmentor on chest x-rays using criss-cross attention and customized radiorealistc abnormalities generation, in: International Conference on Medical Imaging with Deep Learning, PMLR. pp. 457–467.

Tarvainen, A., Valpola, H., 2017. Mean teachers are better role models: Weight-averaged consistency targets improve semi-supervised deep learning results. arXiv preprint arXiv:1703.01780.

Ulyanov, D., Vedaldi, A., Lempitsky, V., 2016. Instance normalization: The missing ingredient for fast stylization. arXiv preprint arXiv:1607.08022.

Van Ginneken, B., Stegmann, M.B., Loog, M., 2006. Segmentation of anatomical structures in chest radiographs using supervised methods: a comparative study on a public database. *Medical image analysis* 10, 19–40.

Xue, Y., Feng, S., Zhang, Y., Zhang, X., Wang, Y., 2020. Dual-task self-

- supervision for cross-modality domain adaptation, in: International Conference on Medical Image Computing and Computer-Assisted Intervention, Springer. pp. 408–417.
- Zhu, J.Y., Park, T., Isola, P., Efros, A.A., 2017. Unpaired image-to-image translation using cycle-consistent adversarial networks, in: Proceedings of the IEEE International Conference on Computer Vision (ICCV).